American Mineralogist, Volume 104, pages 1117–1130, 2019

Monazite and xenotime solubility in hydrous, boron-bearing rhyolitic melt

Monika K. Rusiecka[1,*] and Don R. Baker[1]

[1]Department of Earth and Planetary Sciences, McGill University, 3450 University Street, Montreal, H3A 0E8 Québec, Canada

Abstract

We conducted a series of monazite and xenotime dissolution experiments in a boron-bearing silicic melt at 1000–1400 °C and 800 MPa in a piston-cylinder apparatus. We present new measurements of monazite and xenotime solubility in hydrous (~3 wt% water), boron-bearing rhyolitic melts, as well as the diffusivities of the essential structural constituents of those minerals (LREE, P, and Y). We compare our results to the previous studies and discuss the implications of this study on the understanding of natural, silicic (granitic/rhyolitic) systems.

We propose one equation describing the relationship between the solubility of xenotime and temperature in hydrous rhyolitic melts:

$$\ln Y = 18.3 \pm 0.3 - \frac{125499 \pm 3356}{RT}$$

and another for monazite:

$$\ln \Sigma \text{LREE} = 18.6 \pm 1.5 - \frac{129307 \pm 18163}{RT}.$$

In the presence of sufficient phosphorous, the concentration of LREE needed for monazite saturation is within the uncertainty of the Y concentration needed from xenotime saturation and indicates that in the case of equilibrium crystallization the mineral that forms will only depend on the availability of LREE and Y and HREE. Given the similarity of the solubility of xenotime to that of monazite, we propose that previously published models of monazite solubility in silicic melts can potentially be applied to xenotime, and could, like monazite, serve as a geothermometer.

In the case of disequilibrium crystallization in front of rapidly growing crystals, Y will diffuse faster than LREE and xenotime will only crystallize when LREE are depleted. We also found that the diffusion of Y is greater than the diffusion of P from dissolving xenotime, unlike the similar diffusivities of LREE and P during monazite dissolution. The significant difference between Y and P diffusivities suggests that the components forming xenotime diffuse as separate entities rather than molecular complexes.

The dissolution of phosphates (monazite, xenotime, apatite) in hydrous, silicic melts with the addition of boron leads to liquid-liquid immiscibility at high temperatures where the saturation values of P and either light rare earth elements or Y are in the weight percent range. Immiscibility is not observable at low, magmatic temperatures, most probably due to the lower concentrations of P_2O_5 necessary for phosphate saturation at these conditions; however addition of other components, notably F, may result in liquid-liquid immiscibility at magmatic temperatures.

Keywords: Monazite solubility, xenotime solubility, silicate melts, LREE diffusion, Y diffusion, liquid-liquid immiscibility

Introduction

Phosphate minerals are ubiquitous hosts of trace elements in felsic rocks and can provide useful record of their petrogenetic history. Three of the common phosphates, apatite, monazite, and xenotime, are important hosts of rare earth elements (REE) and yttrium (Y), as well as uranium (U) and thorium (Th). Apatite is the most common of these minerals, however many felsic magmas contain insufficient calcium for apatite saturation, and instead monazite or xenotime crystallize. Monazite and xenotime are common REE-rich phosphates in felsic rocks and can be found in both in granites and granitic pegmatites (Rapp and Watson 1986; Hulsbosch et al. 2014; Guastoni et al. 2016). Monazite, with a monoclinic structure, preferentially incorporates light rare earth elements, LREE (La-Gd), in a $REEO_9$ polyhedron, whereas xenotime, with a tetragonal structure, preferentially incorporates Y and heavy rare earth elements, HREE (Tb-Lu), in a $REEO_8$ polyhedron (Ni et al. 1995). The presence of either of these crystals controls the budget of REE, Y, U, and Th in felsic magmatic systems (i.e., Miller and Mittlefehldt 1982, 1983; Rapp

* E-mail: monika.rusiecka@mail.mcgill.ca

0003-004X/19/0008–1117$05.00/DOI: https://doi.org/10.2138/am-2019-6931

and Watson 1986). Additionally, monazite saturation has been suggested as a possible geothermometer (Montel 1993; Skora and Blundy 2012; Stepanov et al. 2012; Duc-Tin and Keppler 2015). Because of U and Th inclusion in their lattices and their resistance to radiation damage and weathering, these minerals are often used for age determinations (i.e., Asami et al. 2002; Suzuki and Kato 2008; Li et al. 2013); therefore, knowledge of the conditions necessary for magma saturation in these minerals will provide a useful addition to age determinations when investigating magmatic evolution.

Many researchers studied the solubility of monazite (i.e., Montel 1986, 1993; Rapp and Watson 1986; Keppler 1993; Stepanov et al. 2012; Duc-Tin and Keppler 2015), but xenotime saturation was determined only in an iron-free, haplogranitic melt at 800 °C and 200 MPa by Duc-Tin and Keppler (2015). Although there exists a plethora of other REE-rich minerals that are occasionally observed in granites and pegmatites (i.e., Bea 1996; Ercit 2005), monazite is a good example of REE-rich minerals because of its ubiquity in felsic rocks. Therefore, much of the understanding of REE behavior in granitic compositions is based upon our knowledge of monazite solubility.

Monazite is a model mineral for all of the REE-rich minerals because its saturation depends upon the concentrations of REE in the melt, which are at parts per million levels, and the concentrations of other elements in the melt (e.g., P, Ca, Si, Ti, Mn) present at much higher levels, from hundreds of parts per million up to the weight percent level. Thus, the saturation of the monazite should critically depend upon the less-concentrated components in the melt, the REE, which are considered essential structural constituents (ESC, a term first used by Sun and Hanson 1975) and must exceed concentrations necessary to saturate the system in a REE-rich mineral. Previous studies demonstrated that monazite crystallization can be represented either by a reaction between oxide species in the melt and crystalline monazite (Rapp and Watson 1986), or a reaction between molecular $REEPO_4$ complexes in the melt and crystalline monazite (Duc-Tin and Keppler 2015). Although these reactions and their equilibrium constants cannot describe the full composition of monazite because this mineral can also incorporate significant concentrations of Ca, Th, Si, and U, these additional elements need not be considered since they are not essential for monazite crystallization.

In this work we present new data on monazite and xenotime solubility in boron-bearing, hydrous rhyolitic melts, as well as the diffusivity of the components of those minerals (LREE, P, and Y). Boron-bearing melts were studied because some granites and granitic pegmatites contain significant concentrations of boron, as evidenced by the presence of tourmaline, which is a pervasive accessory mineral in many of them. The effect of boron on melts of granitic composition has been reported in multiple studies (i.e., Chorlton and Martin 1978; Pichavant 1981, 1987; Dingwell et al. 1992; Holtz et al. 1993). These studies concluded that boron lowers the solidus and liquidus temperatures of granitic melts; for example, Pichavant (1981) reported a solidus temperature drop in a haplogranitic melt of ~30 °C with the addition of 2 wt% B_2O_3, ~60 °C with 5 wt% B_2O_3, and ~130 °C with 17 wt% B_2O_3. The addition of boron, along with the lowering solidus and liquidus temperatures, increases the solubility of water in the melt (Pichavant 1981; Holtz et al. 1993) and lowers the melt viscosity, affecting generation, extraction, and migration of magmas from their sources (Bartels et al. 2013). These effects of boron motivated this study of the possible effects of boron on the solubility of monazite and xenotime in rhyolitic melts.

In this contribution, the influence of boron on the solubility of monazite and xenotime is presented and compared to previous studies, and its implications on the understanding of processes in natural, silicic (granitic/rhyolitic) magmatic systems is discussed.

Experimental procedures

Monazite and xenotime solubility experiments were conducted in a piston-cylinder apparatus at 800 MPa and temperatures from 1000 to 1400 °C by studying the dissolution of single crystals into a B-enriched rhyolitic melt, following the techniques of Rapp and Watson (1986).

Three different starting compositions were used: LCOB2 = with the addition of 332 ppm B, LCOB3 = with 201 ppm B, and LCOB4 = with 70 ppm B. Additionally, we conducted one experiment (LCOMS) on the solubility of monazite in rhyolitic melt without the addition of boron. The initial starting material was prepared by crushing and grinding rhyolitic obsidian from Lake County, Oregon, with the addition of 332 ppm B as B_2O_3 (LCOB2) followed by melting for 4 h at 1400 °C and grinding. The two other starting glasses (LCOB3 and LCOB4) were prepared by mixing LCOB2 with pure obsidian powder to dilute the concentration of B to those of LCOB3 and of LCOB4. After mixing, all three powders were melted twice more in air at 1400 °C for 4 h with grinding in a Spex mill between fusions. The typical B concentration in granite varies between 0 and 50 ppm (GeoRoc database, http://georoc.mpch-mainz.gwdg.de/georoc/, accessed Dec. 4, 18) and LCO has 22 ppm B. However, some silicic rocks, for example, granitic pegmatites can be significantly more enriched in boron (e.g., Mt Mica, Maine, U.S.A. has 287 ppm B, Simmons et al. 2016), and the concentrations of B in the starting materials were chosen to represent enriched felsic melts. Natural monazite crystals from Vicente Marinho, Minas Gerais, Brazil, xenotime from an unknown locality in Brazil, and apatite from Durango, Mexico, were used for the experiments. Crystals were polished on one side and cut into ~1 mm^3 cubes. Compositions of these glasses and crystals are presented in Table 1.

Platinum capsules (9 × 3 mm in diameter) were prepared by adding water, then rock powder then a monazite or xenotime cube and, then filled with rock powder on top (Fig. 1a). Capsules were welded under water to prevent water loss. Next, the capsules were put in the oven at 110 °C for at least an hour to check for leaks. Capsules were placed into holes drilled into crushable alumina pieces of the piston-cylinder assemblies. The free space around the capsules was filled with pyrophyllite or alumina hydroxide powder (the latter only for experiments at 1300 and 1400 °C), placed on top of a Pyrex base and surrounded by a graphite furnace, which was surrounded by Pyrex and NaCl outer sleeves (Fig. 1b). The capsules

Table 1. Composition of starting materials

Crystals	MNZ	s.d.		XNO	s.d.	
SiO_2	1.92	0.11	P_2O_5	37.05	0.15	
P_2O_5	28.84	1.67	Y_2O_3	45.80	1.20	
CaO	1.04	0.06	Gd_2O_3	4.65	1.07	
La_2O_3	10.34	0.60	Dy_2O_3	7.34	0.45	
Ce_2O_3	26.57	1.54	Er_2O_3	3.60	0.31	
Pr_2O_3	2.90	0.17	Yb_2O_3	1.56	0.23	
Nd_2O_3	11.56	0.67	Total	98.44		
Sm_2O_3	3.37	0.20				
ThO_2	13.18	0.77				
UO_2	0.28	0.02				
Total	100.00					
Glasses	**LCOB2**	**s.d.**	**LCOB3**	**s.d.**	**LCOB4**	**s.d.**
SiO_2	76.72	1.01	75.41	0.88	75.35	0.57
TiO_2	0.07	0.21	0.05	0.14	0.21	0.09
Al_2O_3	13.33	0.41	13.26	0.24	13.29	0.31
FeO	0.52	0.25	1.21	0.37	1.41	0.29
MgO	0.06	0.04	0.04	0.05	0.03	0.04
CaO	0.78	0.09	0.83	0.09	0.78	0.08
Na_2O	3.60	0.17	3.37	0.25	3.38	0.23
K_2O	4.77	0.21	4.68	0.14	4.64	0.08
P_2O_5	0.01	0.00	0.01	0.00	0.01	0.00
Total	99.86		98.86		99.10	
B ppm	332	22	201	9	70	3
Li ppm	55	2	58	3	58	2

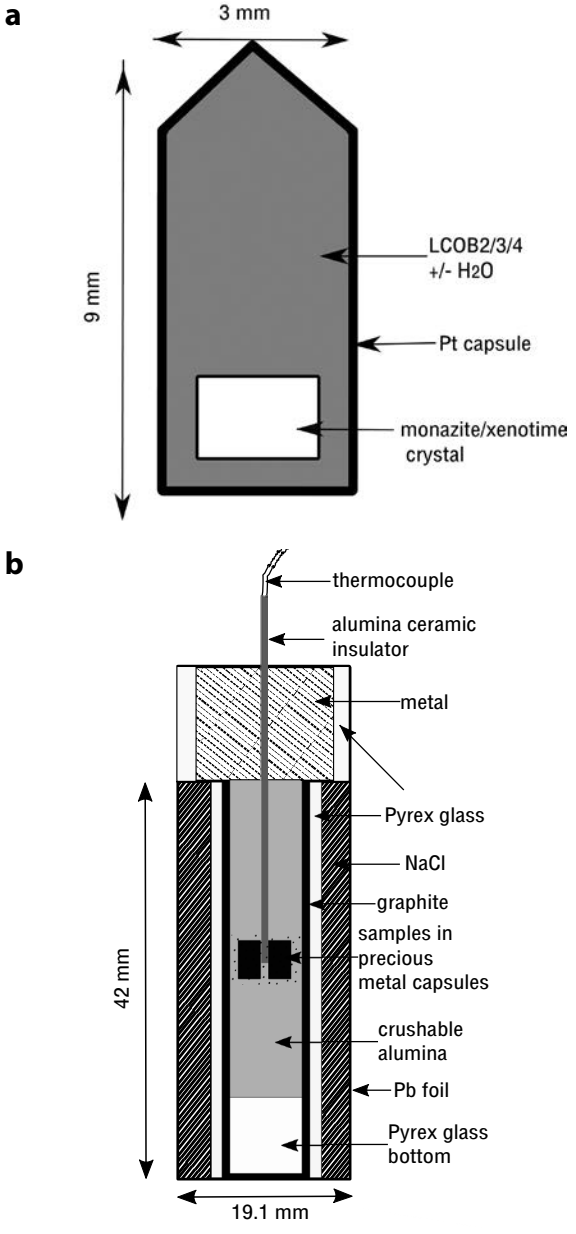

Figure 1. (**a**) Schematic diagram of the experimental capsule for the monazite solubility experiments. (**b**) Cross section of piston cylinder assembly used in this study.

were oriented with the crystals at the base during the experiment to prevent the crystal from sinking. Temperature was controlled by tungsten-rhenium (type C) thermocouples, and the temperature gradients along the capsules were less than 10 °C (Hudon et al. 1994). The heating rate was 100 °C/min. Oxygen fugacity was not controlled, but the intrinsic oxygen fugacity of the assembly was previously determined to be approximately two log units above the Ni-NiO buffer (e.g., Dalpé and Baker 2000). All experiments were quenched isobarically to avoid the formation of bubbles.

Analytical procedure

After each experiment, the run products were placed in epoxy, ground to approximately half the capsule diameter and polished. Raman spectroscopy, scanning electron microscopy, and electron microprobe analysis were used to characterize the run products formed in the experiments.

Water concentrations were determined by Raman spectroscopy following the method of Behrens et al. (2006) and Fortin et al. (2015). Raman spectra were collected at McGill University using a Renishaw InVia confocal micro-Raman spectrometer with a 532 nm laser and 100× Leica microscope objective. The power was set to 10% (50 mW), and a 2400 L/mm grating system with a 50 μm slit was used. The spectra were recorded using Wire 4.2 software. The acquisition time was set to 40 s and repeated 5 times. The uncertainty was calculated as a standard deviation of the calculated water concentrations of the glass standards used in the analyses from the water concentrations measured by ion microprobe.

The backscattered electron (BSE) images were collected at McGill University using a Hitachi SU5000 scanning electron microscope (SEM). The accelerating voltage was 5, 10, or 15 kV depending on the sample. The chemical analyses were performed at McGill University using Cameca SXFiveFE Electron Probe Microanalyzer at a 10 kV accelerating voltage and 50 nA beam current. The major elements were analyzed with counting time of 10 s on the peak and 5 s on the background; the counting time for phosphorus was 120 s on the peak and 60 s on the background, and for rare earth elements the counting times were 240 s on the peak and 120 s on the background. The standards used were a rhyolite glass for Si and K; albite for Na; and a basalt glass for Ti, Al, Fe, Mg, and Ca. A P-bearing glass and REE glasses were used as standards for P and REE. Xenotime and monazite analyses used apatite as the P and Ca standard; diopside was the standard for Si, and the standards for Th and U were ThO_2 (thorianite) and UO_2 (uraninite). REE and P concentration gradients perpendicular to the crystal/glass interface were measured in each experiment. For early experiments multiple traverses were analyzed and because they yielded the same results (within uncertainty) in later experiments only one traverse per sample was analyzed.

Boron and lithium in starting glasses and in pure LCO were analyzed by laser ablation-inductively coupled plasma-mass spectrometry (LA-ICP-MS) at the radiogenic and non-traditional stable isotope geochemistry laboratory at Geotop/Université du Québec à Montréal using a Nu AttoM double-focusing, high-resolution inductively coupled plasma mass spectrometer. The instrument was operated in linked-scan mode in combination with a Photon Machine G2 laser ablation system using a 193 nm wavelength. The laser spot was 85 μm in diameter to increase sensitivity. The NIST-610 glass standard was analyzed as the reference. The concentration of Li and B from time-resolved data collected on the spectrometer were calculated with the use of the IS trace element data reduction scheme built in the Iolite software (Paton et al. 2011) with ^{27}Al as the internal reference (the concentration of Al was determined from EPMA analyses of the glasses).

The electron microprobe analytical traverses were used to determine the concentration at the crystal/melt interface, the saturation concentration, as well as the diffusivity of P and either REE or Y through use of the solution to the second Fick's law for a thick source in semi-infinite medium with the crystal/melt (glass) interface treated as fixed plane at $x = 0$ (Crank 1975):

$$\frac{C - C_1}{C_0 - C_1} = \mathrm{erf}\,\frac{x}{2\sqrt{Dt}} \quad (1)$$

where C is the concentration at distance x from the crystal/melt interface at time t, C_0 is the initial concentration (background), and C_1 is the concentration at the interface (concentration at saturation state). The diffusivity (D) and crystal/melt interface concentration were calculated by fitting analytical data obtained from microprobe traverses for each temperature to Equation 1 linearized by inversion of the error function (Fig. 2, Eq. 2) and considering $C_0 = 0$ (cf. Rapp and Watson 1986):

$$\mathrm{erf}^{-1}\left(1 - \frac{C}{C_1}\right) = \frac{x}{\sqrt{4t}}\frac{1}{\sqrt{D}} \quad (2)$$

We also performed a series of nonlinear fits to Equation 1 using the Matlab "cftool" and compared these results to the results of linearized fitting (Eq. 2). The values obtained for crystal/melt interface and diffusivity by nonlinear fitting of Equation 1 agree with those calculated from Equation 2 to within uncertainty. Moreover, a significant portion of this research is the comparison of our results with the results of Rapp and Watson (1986) and therefore, in our opinion, using the same technique as they used for fitting analytical data is rational.

The uncertainties of diffusivities and concentrations at the crystal/melt interface for each sample were calculated from 95% confidence bounds of the fit.

To account for the fluorescence effect from the crystals, the first analysis considered when calculating diffusion coefficients and concentrations of LREE and P at the crystal/melt interface was taken ~20–30 μm away from the crystal following the procedure established by Rapp and Watson (1986) and Duc-Tin and Keppler (2015).

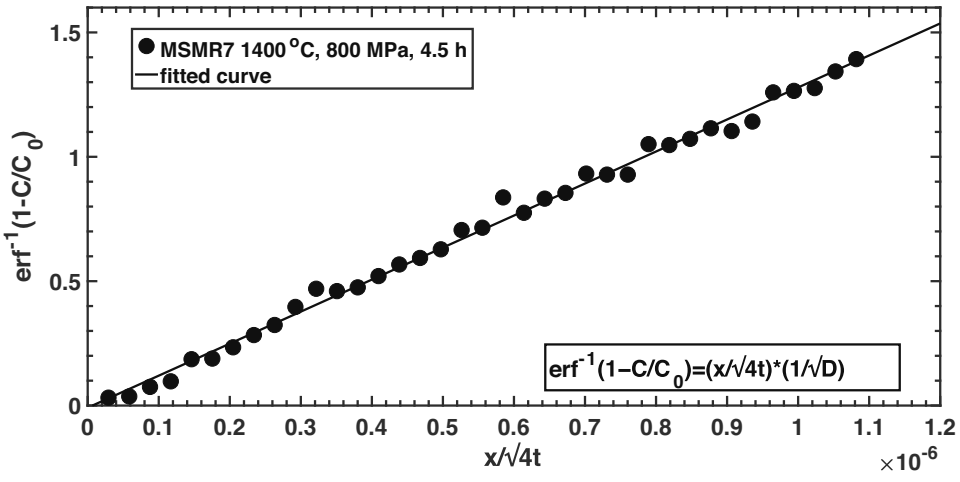

FIGURE 2. Fit of experimental data to inverted error function $\text{erf}^{-1}\left(1-\frac{C}{C_1}\right)=\frac{x}{\sqrt{4t}}\frac{1}{\sqrt{D}}$ where C is the concentration at distance x from the crystal/melt interface for experimental duration t, C_1 is the concentration at the interface (concentration at saturation state), and D is diffusivity.

RESULTS

Nanoparticles near the crystal-melt interface

During routine analysis of the run products for water concentrations, an interesting feature in the Raman spectra of glass neighboring the monazite crystals was noted. Spectra showed bands characteristic of crystalline monazite rather than silicate glass (Fig. 3).

The band around 975 cm^{-1} visible both in monazite and glass spectra is assigned to symmetric stretching of a PO_4 molecule (Silva et al. 2006). The band around 1060 cm^{-1} is assigned to asymmetric stretching of a PO_4 molecule. Two other bands connected to PO_4 bending are present in monazite spectrum—around 470 cm^{-1} (symmetric) and around 640 cm^{-1} (asymmetric). The 470 cm^{-1} band seems to be visible in the glass, however in the spectrum furthest away from the crystal this band appears to be covered by a silicate glass band. The 640 cm^{-1} band appears to be shifted to higher values in the glass spectra when compared to the monazite spectrum. The remaining bands are attributed to complex lattice modes that involve interaction between $REEO_9$ polyhedra with PO_4 tetrahedra (Silva et al. 2006).

The samples showing monazite features in Raman spectra of the glasses were further investigated by scanning electron microscope. Backscattered electron imaging revealed the presence of a nanoparticle zone, or moat, around the dissolving monazite crystal (Fig. 4a) in two experiments, one conducted at 1400 °C, 800 MPa for 4.5 h and another at 1300 °C, 800 MPa for 20 h. The same nanoparticle moats can be observed in one experiment on xenotime solubility at 1400 °C in melts containing boron. A similar experiment to those containing monazite or xenotime but using apatite was performed at 1400 °C, 800 MPa for 4.5 h with the addition of boron, and in this experiment the nanoparticle moat was also observed.

Close inspection of the particles revealed that they are spherical droplets rich in P and REE (Fig. 4a), hosting smaller droplets of different composition with a lower mean atomic weight (Fig. 4b). Attempts to analyze the droplets were unsuccessful because of their small dimensions, even using the field emission guns on the SEM and the electron microprobe. However, the nanoparticles are clearly enriched in P and LREE, and the grayscale value of the smaller droplets inside the particles is similar to the LCO glass (Fig. 4b), leading us to interpret them as silicate glass. The presence of the secondary, presumably silicate, phase within the P-rich nanoparticles is consistent with an interpretation that they represent liquid-liquid immiscibility that quenched to crystalline monazite (or monazite-like phosphates) at room temperature, as evidenced by the Raman spectra (Fig. 3). The morphology of the nanoparticles (Fig. 4b) and their presence in multiple experiments of different durations (Table 2) suggests that they were formed by equilibrium liquid-liquid immiscibility due to the diffusion of P and REE (or Y) into the B-bearing rhyolite melt. The nanoparticle zone was also observed in the boron-free experiment (LCOMS) at 1400 °C, however the width of the moat and the diameters of the nanoparticles are significantly (over 3 times) smaller than in the boron-bearing runs (~100 μm in boron-bearing and ~30 μm in boron free experiment).

To investigate whether the nanoparticles were an equilibrium or quench phenomenon, we calculated the duration of diffusion limited growth of a spherical particle (modified after Berner 1968) of the same size as the nanoparticles. We considered a sphere 200 nm in diameter (average size of a nanoparticle in the moat region) and assumed a composition of equivalent to monazite. The diffusivities necessary for this calculation were taken from the results of this study (presented below). From the calculation, we estimated that it would take approximately 4 min to form a particle of that size, whereas the duration of the quench was less than 1 min. We therefore hypothesize that formation of those particles during quench is unlikely.

Figure 4a shows that the phosphate-rich nanoparticle zones do not start at the crystal/glass (melt) interface but are separated from the monazite crystal by a thin (~3 μm in the experiment at 1400 °C and ~2 μm in the experiment at 1300 °C) layer without nanoparticles. The chemical composition of the nanoparticle-rich zone is different from that of the glass beyond that zone, not only

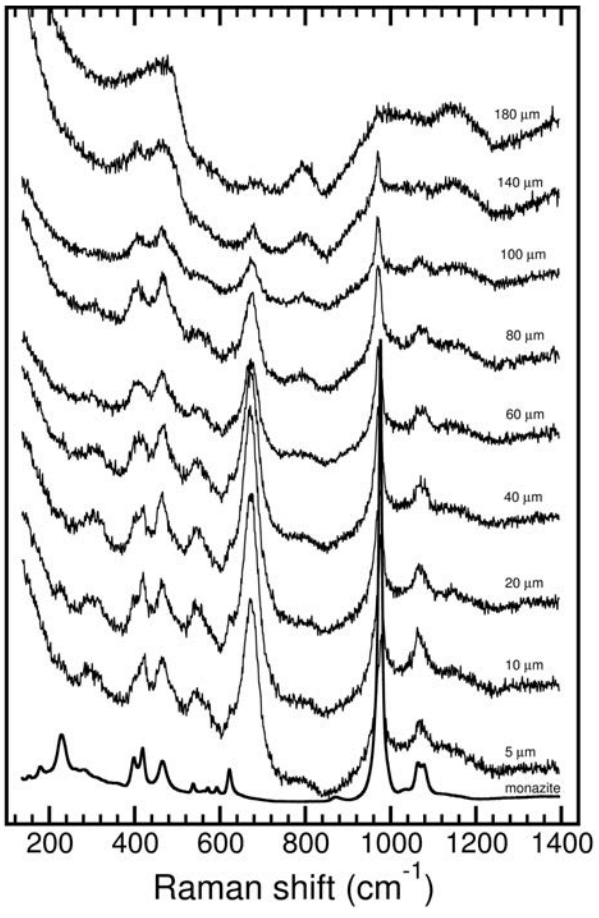

Figure 3. Raman spectra of sample MSMR8 (1400 °C, 800 MPa, 4.5 h) including spectrum of monazite crystal and spectra of adjacent glass at distances of 5 to 180 μm away from the crystal/melt interface. From 5 to 100 μm the spectra are dominated by features visible in monazite spectrum; beyond 100 μm the aluminosilicate glass features become dominant.

with respect to P and light rare earth elements (LREE) but also to major element components of the glass. For example, a plot of CaO and FeO vs. distance from the monazite/melt interface in experiment MSMR7 at 1400 °C demonstrates an enrichment of CaO and FeO at the crystal-melt interface relative to the glass further away from the crystal (Fig. 5). The concentration of FeO and CaO stabilizes to the concentration in the LCOB starting material at approximately 100 μm away from the crystal. This enrichment in the moat region is caused by CaO and FeO diffusing from the silicate melt to the phosphate-rich melt. The uphill diffusion of FeO seen in Figure 5 would not be expected if the concentrations of FeO displayed in Figure 5 were a function of analyzing different fractions of a mixture of homogeneous phosphate nanoparticles and homogeneous silicate glass. The differences in FeO and CaO concentrations between the moat and LCOB demonstrate that the melt at the crystal interface is no longer the rhyolitic melt used as a starting material. Because of this compositional change, monazite at the crystal/melt interface is no longer dissolving into LCO rhyolitic melt.

The nanoparticle moat in experiments at 1300 and 1400 °C presents a challenge for the determination of monazite and xenotime saturation concentrations and mobility of P and REE (and Y in the xenotime dissolution experiments) in a rhyolitic melt. To circumvent the inability of analyzing only silicate glass in the moat, diffusivities and crystal solubilities in experiments at 1300 and 1400 °C were determined by using only analyses further away from the crystals than the outer edge of the phosphate nanoparticle moat. Treating the data in this manner involves the explicit hypothesis that the nanoparticles are equilibrium immiscible liquids, that the silicate liquid at the outer edge of the moat is in equilibrium with the nanoparticles, and that the nanoparticles are in equilibrium with the monazite. Although this equilibrium may only be a transient equilibrium (cf. Watson 1982), the data treatment used provides the best approximation of the true values. If the nanoparticles are not an equilibrium immiscible liquid but instead are a non-equilibrium immiscible liquid formed during quench or crystalline monazite (or xenotime), then neglecting analyses in the nanoparticle moat

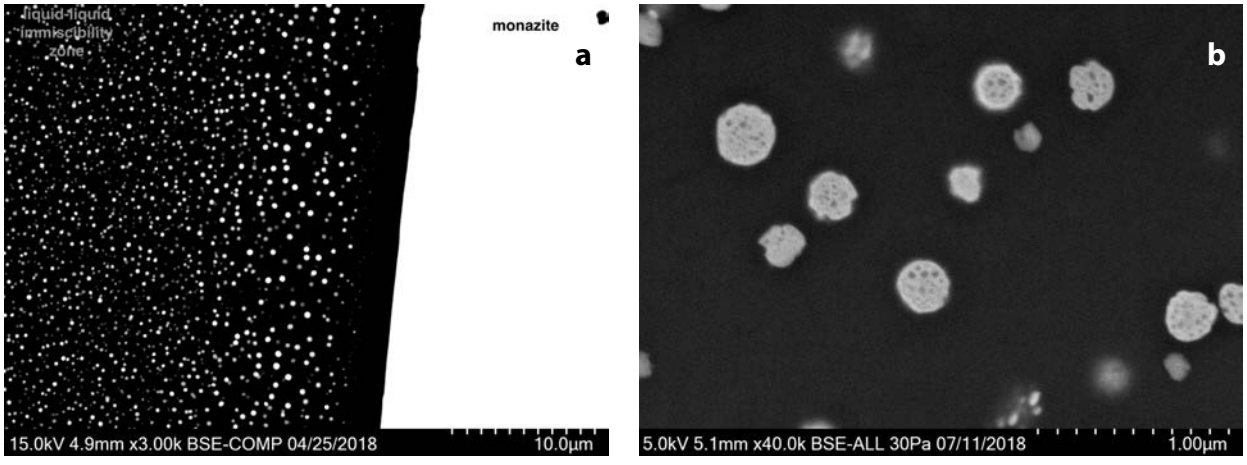

Figure 4. (**a**) SEM-BSE image of sample MSMR8 (1400 °C, 800 MPa, 4.5 h) showing the presence of the liquid-liquid immiscibility zone with phosphate nanocrystals (bright, spherical phase) and the quenched silicate glass (dark gray) next to the dissolving monazite crystal. (**b**) Backscattered electron image of sample MSMR8 (1400 °C, 800 MPa, 4.5 h) showing a few bright nanocrystals in the quenched glass at high magnification. Note the presence of dark gray inclusions in the nanocrystals interpreted as quenched silicate glass.

TABLE 2. Experimental run table

Xenotime run	B (ppm)	T (°C)	Duration (h)	Duration (s)	H_2O (wt%)	D^P (m^2/s)	C_0 (wt% P_2O_5)	D^Y (m^2/s)	C_0Y (ppm)
XSMR7	332	1000	72	259200	1.5 ± 0.05	$1.0^{-0.9}_{+0.4}\times10^{-13}$	$0.19^{+0.02}_{-0.02}$	$1.1^{-0.09}_{+0.08}\times10^{-13}$	660^{+165}_{-540}
XSMR5	201	1200	54	194400	2.5 ± 0.08	$2.4^{-0.16}_{+0.14}\times10^{-13}$	$0.75^{+0.04}_{-0.04}$	$1.3^{-0.4}_{+0.3}\times10^{-12}$	3100^{+380}_{-600}
XSMR12	70	1400	4.5	16200	3.2 ± 0.11	$6.0^{-1.5}_{+1.1}\times10^{-13}$	$1.6^{+0.3}_{-0.5}$	$2.6^{-0.5}_{+0.4}\times10^{-12}$	11300^{+1250}_{-1800}
Monazite run	**B (ppm)**	**T (°C)**	**Duration (h)**	**Duration (s)**	**H_2O (wt%)**	**D^P (m^2/s)**	**C_0 (wt% P_2O_5)**	**D^{LREE} (m^2/s)**	**C_0LREE (ppm)**
MSMR10	332	1000	70	252000	2.7 ± 0.09	$2.6^{-1.6}_{+13}\times10^{-14}$	$0.13^{+0.01}_{-0.01}$	$7.7^{-2.6}_{+4.4}\times10^{-14}$	824^{+113}_{-206}
MSMR19	332	1000	148.9	536040	2.6 ± 0.09	$5.8^{-2.9}_{+11}\times10^{-14}$	$0.08^{+0.03}_{-0.3}$	$0.5^{-0.3}_{+1.6}\times10^{-14}$	1730^{+824}_{-1030}
MSMR13	332	1100	72	259200	3 ± 0.10	$5.1^{-0.5}_{+0.6}\times10^{-14}$	$0.19^{+0.02}_{-0.03}$	–	1139^{+185}_{-142}
MSMR22	332	1300	20	72000	3.5 ± 0.12	$2.9^{-0.7}_{+1.1}\times10^{-14}$	$0.44^{+0.08}_{-0.2}$	$2.8^{-0.9}_{+6.0}\times10^{-13}$	4800^{+1820}_{-4700}
MSMR7	332	1400	4.5	16200	2.5 ± 0.08	$1.9^{-0.3}_{+0.3}\times10^{-13}$	$0.85^{+0.16}_{-0.26}$	$8.3^{-3.3}_{+12}\times10^{-13}$	16369^{+3943}_{-14617}
MSMR3	201	1200	33	118800	1.7 ± 0.06	$6.1^{-0.4}_{+0.3}\times10^{-13}$	$0.35^{+0.01}_{-0.01}$	$8.9^{-4.6}_{+4.6}\times10^{-13}$	3035^{+203}_{-178}
MSMR8	201	1400	4.5	16200	2.8 ± 0.09	$1.2^{-0.2}_{+0.2}\times10^{-13}$	$1.45^{+0.34}_{-0.62}$	$7.8^{-3.6}_{+2.1}\times10^{-13}$	26780^{+6000}_{-13220}
MSMR6	70	1200	54	194400	4 ± 0.14	$2.0^{-0.1}_{+0.1}\times10^{-13}$	$0.41^{+0.03}_{-0.03}$	$1.6^{-1.1}_{+5.3}\times10^{-13}$	2500^{+550}_{-1600}
MSMR9	70	1400	4.5	16200	3.7 ± 0.13	$1.4^{-0.5}_{+0.3}\times10^{-13}$	$1.25^{+0.4}_{-1.04}$	$1.1^{-1.3}_{+0.3}\times10^{-12}$	23200^{+7328}_{-4080}
LCOMS	22	1400	4.5	16200	1.7 ± 0.06	$7.25^{-0.48}_{+0.43}\times10^{-13}$	$0.88^{+0.09}_{-0.07}$	$2.12^{-0.5}_{+0.8}\times10^{-12}$	8137^{+1504}_{-2843}

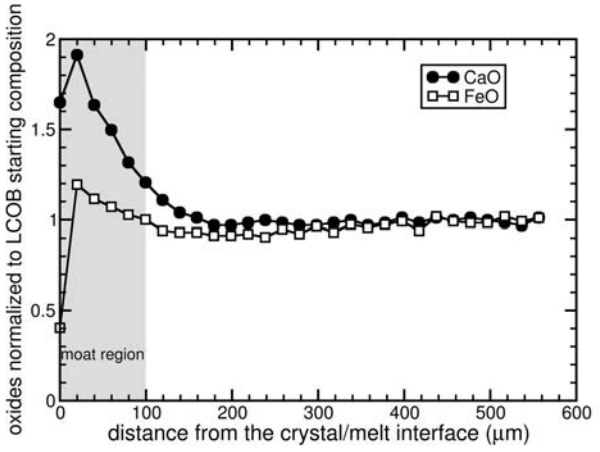

FIGURE 5. CaO and FeO normalized to concentrations more than 1 mm away from the dissolving crystal vs. distance from the crystal/melt interface for the sample MSMR9 (1400 °C, 800 MPa, 4.5 h). Note the appearance of uphill diffusion in the moat region (liquid-liquid immiscibility zone).

remains an appropriate technique for the determination of diffusivities and solubilities in the rhyolitic melt investigated.

Experiments at temperatures below 1300 °C did not produce a nanoparticle zone and therefore their diffusion profiles starting from a distance of 20 to 30 μm away from the crystal-melt interface were used for diffusivity and solubility determinations. Interestingly, the nanoparticle moat in the boron-free monazite dissolution experiment (LCOMS) at 1400 °C is only 30 μm wide, which means that its presence had no influence on the diffusion profile and solubility of P and LREE at monazite saturation calculated from the concentration profiles in our work and in that of Rapp and Watson (1986).

Diffusion of monazite and xenotime components

Figure 6 compares diffusion profiles of REE, P, and Y for monazite and xenotime starting from the crystal/melt interface and starting from the point where the liquid-liquid immiscibility is no longer observed. Diffusivities of those components, corrected for the presence of the liquid-liquid immiscibility moat zone, were used to calculate the activation energy (E_a) and frequency factor (D_0) for the diffusion of P, LREE, and Y in rhyolitic melt and construct Arrhenius diagrams of diffusion of monazite and xenotime components from dissolving crystals into the melt.

The activation energy for the diffusion of P during monazite dissolution in melt containing 332 ppm B and 3.2 wt% water is 131.4 ± 35.9 kJ/mol. The frequency factor in this case is $D_0 = 0.32^{-0.3}_{+5.6}\times10^{-8}$ m^2/s. The corrected value for theee activation energy of diffusion of the sum of LREE is $E_a = 224.9 \pm 38$ kJ/mol and $D_0 = 0.16^{-0.16}_{+3.3}\times10^{-4}$ m^2/s. The activation energy corrected for the presence of liquid-liquid immiscibility for the diffusion of P from dissolving xenotime is $E_a = 75.6^{+5.8}_{-4.9}$ kJ/mol and the $D_0 = 1.2^{-0.5}_{+1.1}\times10^{-10}$ m^2/s. For diffusion of Y, $E_a = 146.4^{+5.8}_{-4.9}$ kJ/mol and $D_0 = 1.2^{-0.5}_{+1.1}\times10^{-7}$ m^2/s.

Figure 7 presents the comparison of diffusivity of phosphorus in melts with different boron concentrations at 1400 °C. The diffusivities in three melts with different boron concentrations are the same within uncertainties. At the concentrations used in this study, boron concentration seems to have no effect on the diffusivity. The same applies to the diffusion of LREE. The monazite solubility experiments were performed before the xenotime solubility ones and showed that varying boron concentrations do not affect diffusivity or solubility; therefore, xenotime solubility experiments were performed only with one boron concentration (one powder for each experiment).

The experimental studies previously conducted on monazite (i.e., Rapp and Watson 1986; Duc-Tin and Keppler 2015) showed that the diffusivity of LREE and P are similar, suggesting that these essential components of monazite diffuse together as molecular complexes. However, the results of this study indicate that diffusion of Y from dissolving xenotime is an order of magnitude faster than that of P, which points to the possibility of xenotime components diffusing as separate entities rather than molecular complexes. No experiments on xenotime solubility in boron free melts were conducted, so it remains unclear if the decoupling of Y from P is an effect of boron in the melt.

As can be seen in Figure 6, REE and P diffusion profiles starting from the end of the liquid-liquid immiscibility zone plot very close to the profile calculated using Equation 1 and the concentration at

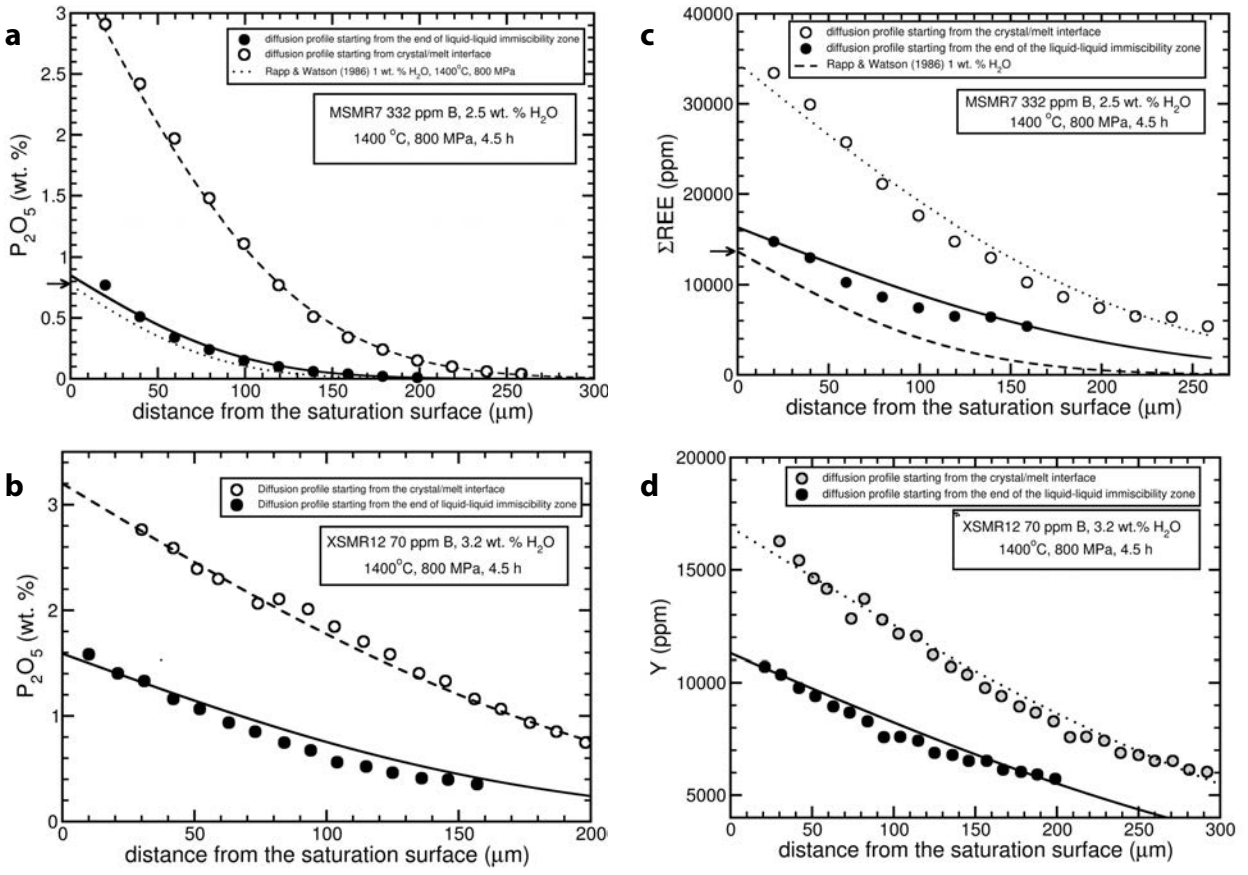

Figure 6. Diffusion profiles of REE, P, and Y for monazite and xenotime starting from the crystal/melt interface and starting from the point where the liquid-liquid immiscibility is no longer observed. (**a**) Diffusion of P (in wt% oxide) from monazite (MSMR7); the arrow points to saturation state value of Rapp and Watson (1986). (**b**) Diffusion of P (in wt% of oxide) from xenotime. (**c**) Diffusion of LREE (in parts per million) from monazite (MSMR7); the arrow points to the saturation state value of Rapp and Watson (1986). (**d**) Diffusion of Y (in parts per million) from xenotime (XSMR12). Supplemental[1] Table S1 with full EPMA traverses for each experiment is available.

crystal/melt interface and diffusivity obtained by Rapp and Watson (1986) (Figs. 6a and 6c). Additionally, the fits to the diffusing species using Equation 1 demonstrate that melt concentrations at the moat-LCO interface are within uncertainty of the P and REE solubility product at monazite saturation calculated by Rapp and Watson (1986) (the y-axis intercept in Fig. 6a and 6c).

Monazite and xenotime solubility

Concentrations of light rare earth elements (ΣLREE) and phosphorus (P) at the crystal/melt interface were used to calculate the [ΣLREE][P] solubility product at monazite saturation (in $mol^2/100g^2$). Despite Ce being the most abundant element in the investigated monazite, the solubility product has been calculated taking into account the sum of the LREE because [Ce] is lower than the sum of all the other LREE. As can be seen in Figure 8a, the apparent solubility product uncorrected for the presence of the nanoparticles at 1300 and 1400 °C in melts with boron is much higher than that of Rapp and Watson (1986); at 1400 °C our results are 1–1.5 orders of magnitude higher. An experiment in LCO without the addition of boron, the same composition as used by Rapp and Watson (1986), was conducted using the same monazite crystal as in experiments with boron addition. The solubility product at monazite saturation for that experiment plots within the uncertainty of the results of Rapp and Watson (1986, Fig. 8a, LCOMS) indicating that the increased monazite solubility results from the boron-enriched melt composition rather than the composition of the dissolving crystal. However, using the corrected profiles at 1300 and 1400 °C with the interface at the moat-LCOB boundary, the solubility product of [LREE][P] (Fig. 8a) is only slightly larger than that measured by Rapp and Watson (1986).

The solubility product of [Y][P] at xenotime saturation has been calculated using yttrium (Y) and phosphorus (P) concentrations at the crystal-melt or moat-melt interface obtained the same way as the values of LREE and P for monazite (Fig. 8a). The concentrations of HREE when compared to Y are much lower (Table 1) and therefore have been treated as non-essential for xenotime. The xenotime measurements at 1400 °C were corrected for the presence of the liquid-liquid immiscibility zone, and Figure 8b shows both the uncorrected and corrected [Y][P] solubility product.

Figure 9 presents the comparison of the [LREE][P] solubility product at monazite saturation and [Y][P] solubility product at xenotime saturation (in $mol^2/100g^2$) as a function of the boron concentration in the melt. As can be seen in Figure 9 the solubility at different boron concentrations at the same experimental

conditions is the same within uncertainty. We only conducted an experiment on xenotime solubility with one boron concentration for each temperature, however, because xenotime solubility similar to monazite solubility it is reasonable to assume that varying boron concentration would also have no effect on [Y][P] solubility product at xenotime saturation.

Discussion

Diffusion of monazite and xenotime components in this and previous studies

Arrhenius plots for the diffusion of P from dissolving monazite (this study and Rapp and Watson 1986), xenotime (this study), and apatite (Harrison and Watson 1984) are presented in Figure 10. The activation energy for the diffusion of P during monazite dissolution in a melt containing 201–332 ppm B and 3.2 wt% waterfalls between the activation energies for P diffusion in rhyolitic melt with 6 and 1 wt% water reported by Rapp and Watson (1986). The diffusion of P from xenotime into a hydrous rhyolitic melt exhibits a lower activation energy than diffusion from monazite (75 kJ/mol for xenotime and 230 kJ/mol for monazite). Diffusion of P from apatite into LCO containing 0.1 wt% H_2O has a much higher activation energy (600 kJ/mol) than diffusion of P from monazite, xenotime, and apatite into hydrous rhyolitic melt (76 to 443 kJ/mol). The diffusion of P from dissolving apatite into LCO melts with 1 or 2 wt% water displays activation energies similar to that for P diffusion from dissolving xenotime. We do not fully understand why diffusion of P from apatite and xenotime into hydrous rhyolitic melt has an activation energy more than 100 kJ/mol lower than from monazite, but we hypothesize that it is due to the fact that diffusion of Ca and P from apatite (Harrison and Watson 1984) and P and Y from xenotime are decoupled, and they do not diffuse as molecular complexes.

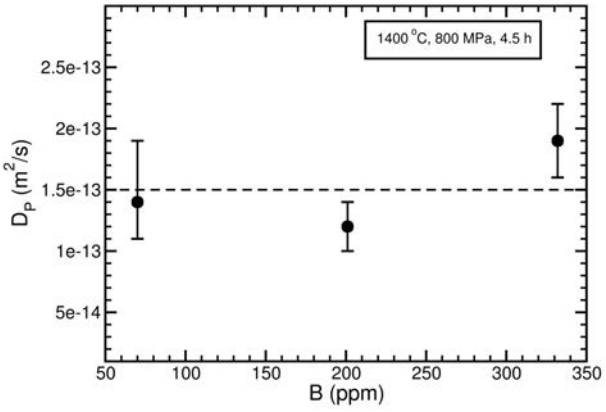

Figure 7. Comparison of the diffusivity of phosphorus in melts from monazite dissolution experiments with different boron concentrations at 1400 °C.

The diffusivities of ΣLREE and Y from different studies are presented in Figure 11. The results of this study show that diffusion of P and Y from xenotime display different activation energies. A similar decoupling was observed by Harrison and Watson (1984) for diffusion of P and Ca from apatite, but during monazite dissolution the diffusivities of P and ΣLREE are similar (Rapp and Watson 1986; this study). The diffusivity of LREE in rhyolite melt with 1 wt% water presented by Rapp and Watson (1986) is

$$D = 2.3\times10^{5}\times\exp\left(\frac{-510.9\,\frac{\text{kJ}}{\text{mol}}}{\text{R}T}\right)$$

and in the same melt with 6 wt% water is

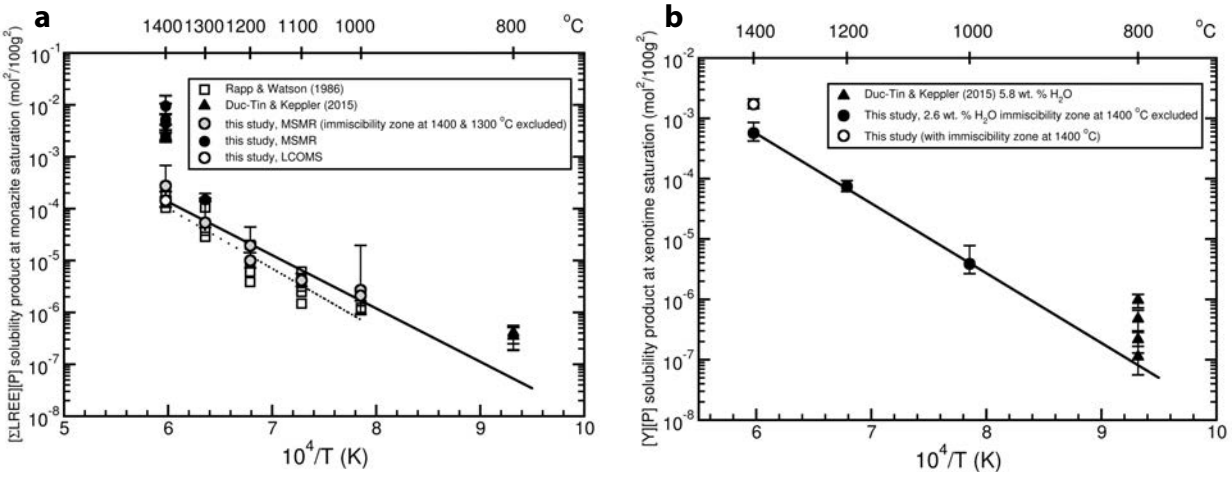

Figure 8. (**a**) [ΣLREE][P] solubility product at monazite saturation ($mol^2/100g^2$). Open square = Rapp and Watson (1986); filled triangle = Duc-Tin and Keppler (2015) phosphates with monazite structure with ASI of 1–1.3; filled gray circles = this study, corrected for the presence of the nanoparticles at 1300 and 1400 °C; filled black circles = this study, uncorrected for the presence of the nanoparticles at 1300 and 1400 °C; open circle = LCOMS from this study, an experiment in LCO without the addition of boron. (**b**) [Y][P] solubility product at xenotime saturation. filled triangle = Duc-Tin and Keppler (2015), average values of solubility of HREE phosphates with xenotime structure in melts with ASI of 1–1.3. Filled circle = [Y][P] solubility product from this study corrected for the presence of immiscibility zone at 1400 °C; open circle = the value of [Y][P] solubility product before correction.

$$D = 0.23 \times \exp\left(\frac{-251.5\frac{\text{kJ}}{\text{mol}}}{\text{R}T}\right)$$

At 1000 °C these equations predict a diffusivity of LREE of 2.5 $\times 10^{-16}$ m^2/s with 1 wt% and 1.1 $\times 10^{-11}$ m^2/s with 6 wt% water. The diffusivity obtained from this study at 1000 °C, 3.2 wt% water, is $6.3^{+3.5}_{-2.1} \times 10^{-15}$ m^2/s, which is consistent with the study of Rapp and Watson (1986) and falls between the values at 1 and 6 wt% water. The similarity of activation energies of P and ΣLREE diffusion away from dissolving monazite in this study and in the study of Rapp and Watson (1986) suggests that boron has no effect on the diffusivity of these elements in rhyolitic melts. Because boron does not have a significant influence on the diffusion of ESC from monazite, we infer the same applies to the diffusion of ESC from xenotime.

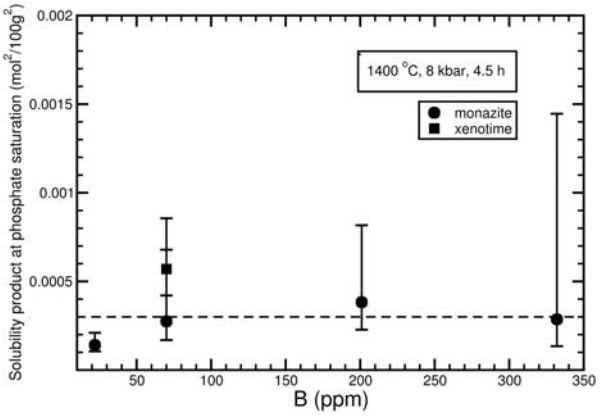

FIGURE 9. Comparison of the [LREE][P] solubility product at monazite saturation and [Y][P] solubility product at xenotime saturation (in mol^2/100g^2) as a function of the boron concentration in the melt.

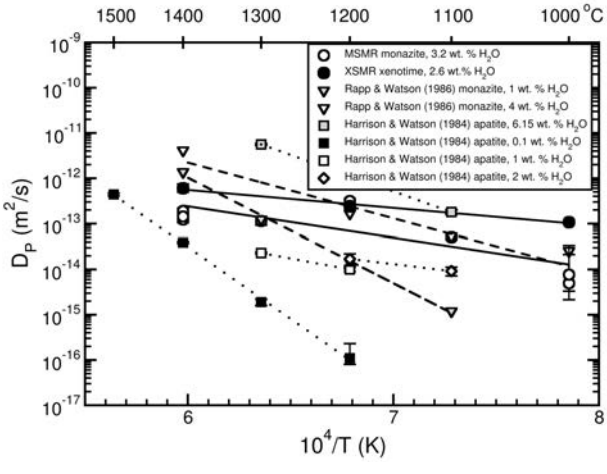

FIGURE 10. Arrhenius plots for diffusion of P from dissolving monazite, this study (filled black circles) and Rapp and Watson 1986 (open circles and filled gray circles), xenotime (this study, filled, black triangles), and apatite (Harrison and Watson 1983, squares and diamonds).

Diffusivities obtained by Holycross and Watson (2018) for both LREE and Y in LCO melt are higher than found in this study. The diffusivities of LREE in the melt with 4 wt% H_2O from the study of Rapp and Watson (1986) also plot below the results of Holycross and Watson (2018), however all of these diffusivities seem to have a similar slope (i.e., similar E_a). Holycross and Watson (2018) also found that Y diffusion is slower than LREE diffusion, whereas this study found that Y diffuses more rapidly than LREE. Although some of these differences between diffusivity measurements in this study and in Holycross and Watson (2018) are possibly due to the higher water concentration in the melts used by Holycross and Watson (4.1 wt% compared to our values of 3.2 and 2.6 wt%), multicomponent diffusion almost certainly contributes to the differences in measured diffusivities. In particular, differences in trace element diffusivities may be attributed to differences in compositional gradients present in the experiments of the two studies. In our study the concentrations of LREE, Y and HREE in the melt are controlled by the dissolution of monazite or xenotime and reach concentrations near 1 wt%, whereas in Holycross and Watson (2018) those elements were added in trace amounts (200–300 ppm) and studied by use of an LCO diffusion couple in which the only compositional gradients were those of the trace elements. Consequently, the trace-element concentration gradients in the study of Holycross and Watson (2018) were significantly lower than concentration gradients created by the dissolution of monazite or xenotime into LCO. These different concentration gradients are the suspected reason behind the differences in measured diffusivities because in multicomponent diffusion the diffusive flux of any individual component is influenced by the chemical potential gradients of all independent components in the system; thus, changes in the concentration gradients affect the measured diffusivities (e.g., Wei and Wuensch 1976; Liang 2010; Guo and Zhang 2016, 2018).

If the differences in measured diffusivities between this study and that of Holycross and Watson (2018) are due to differences in the concentrations of trace elements, then studies using diffusion couples with no major element concentration gradients (as in Holycross and Watson 2018) and high trace element concentrations (as in this study) would be expected to produce results intermediate between those of Holycross and Watson (2018) and of this study. The study that most closely approximates this test is Mungall et al. (1999) that investigated Y diffusion between haplogranitic melts in which one half of the diffusion couple was enriched in Y to ~700 ppm. Although not an ideal test of the effects of multicomponent diffusion on Y diffusion, the results from Mungall et al. (1999) appear intermediate between the results of this study and the results of Holycross and Watson (2018) and support our hypothesis (Fig. 11).

Holycross and Watson (2018) noted differences between measurements of zirconium diffusion in their study at trace concentrations and in the zircon dissolution study of Harrison and Watson (1984) at much higher Zr concentrations in the melt, similar to the differences between LREE and Y in this investigation and in that of Holycross and Watson (2018). As Holycross and Watson (2018) discussed, crystal dissolution experiments may better study diffusion behavior of trace elements near trace-element rich crystals where concentrations are high, whereas the

study of Holycross and Watson (2018) models the behavior of trace elements at lower magmatic concentrations more typically found far from growing crystals.

Effect of temperature on monazite and xenotime solubility

Monazite and xenotime solubility demonstrate clear dependence of solubility on temperature. The solubility of both phosphates increases two orders of magnitude from 1000 to 1400 °C (Figs. 8a and 8b). Published studies of monazite solubility demonstrate similar results and have provided equations to model monazite solubility as a function of pressure, temperature, and melt composition (i.e., Montel 1986, 1993; Rapp and Watson 1986; Keppler 1993; Stepanov et al. 2012; Duc-Tin and Keppler 2015).

Based on the experimental data on the solubility of monazite corrected for the presence of liquid-liquid immiscibility at 1300 and 1400 °C, we derive the following equation for the solubility of monazite in silicic (granitic/rhyolitic) melts with ~3 wt% water presuming that sufficient phosphorous is available for monazite saturation:

$$\ln\Sigma\mathrm{LREE} = 18.6 \pm 1.5 - \frac{129307 \pm 18163}{\mathrm{R}T} . \quad (3)$$

The equation for xenotime solubility is given by:

$$\ln Y = 18.3 \pm 0.3 - \frac{125499 \pm 3356}{\mathrm{R}T} . \quad (4)$$

(We recognize that the precision of our equation may not exceed four significant digits, however, we retain six digits to avoid errors stemming from rounding.) The similarity of these equations for monazite and for xenotime solubility demonstrates that the temperature dependence of both minerals is the same within uncertainty and indicates that in case of equilibrium crystallization the relative concentrations of Y and HREE vs. LREE will be the main control determining which phosphate crystallizes.

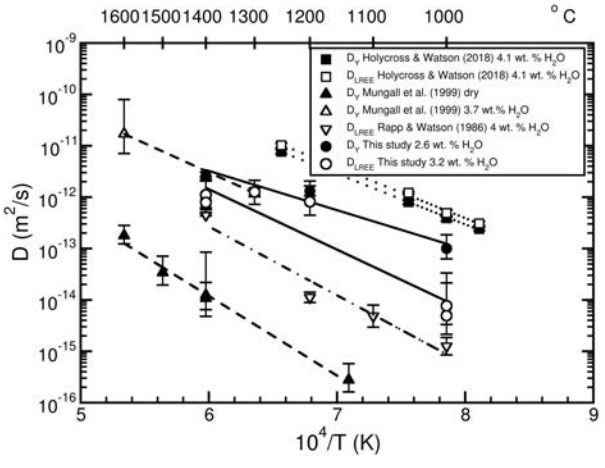

Figure 11. Arrhenius plots for diffusion of ΣLREE and Y from different studies. Squares = Holycross and Watson (2018) (filled = Y, open = LREE); triangle up = Y, Mungall et al. (1999) (filled = dry, open = hydrous melt); triangle down = LREE, Rapp and Watson (1986); circles = this study (filled = Y, open = LREE).

We compared the calculated concentrations of the sum of LREE in a melt saturated with monazite at 1000 °C using several models (Rapp et al. 1987; Montel 1993; Stepanov et al. 2012) with the measured values in this study (Fig. 12). The closest model result is that of Stepanov et al. (2012), which takes into account temperature, pressure, water content and melt composition (but does not consider B, which, as shown above does not influence the saturation of the studied phosphates).

The concentration of Y in a xenotime-saturated melt at 1000 °C, 800 MPa, and 1.5 wt% H_2O was compared to predictions from the three monazite saturation models (Rapp et al. 1987; Montel 1993; Stepanov et al. 2012) by equating the modeled concentration of LREE to the experimentally measured concentration of Y. The Y concentration obtained from the experiments on xenotime solubility at 1000 °C, 800 MPa, and 1.5 wt% H_2O (660 ppm, Table 2) is lower than those predicted by the monazite models, but still within the uncertainty of the solubility model of Stepanov et al. (2012), 734 ppm.

To the best of our knowledge the only study on the solubility of xenotime in silicic melts is that of Duc-Tin and Keppler (2015). However, because the scope of their study was the origin of the lanthanide tetrad effect, they did not study the saturation of silicic melts with pure yttrium phosphate xenotime. Because of the lack of a value for Y phosphate saturation for comparison with our study, we used the value of the average solubility from all the HREE investigated by Duc-Tin and Keppler (2015). Figure 8b compares xenotime solubility measured by Duc-Tin and Keppler (2015) by plotting [ΣHREE][P] in melts with an aluminum saturation index, ASI, similar to LCO (the ASI of LCO is 1.02) from their study with the results of our study extrapolated to the temperature of their experiments. The xenotime solubility products measured by Duc-Tin and Keppler are similar to those predicted by the down-temperature extrapolation of the results of this study. The small differences between the results of the two studies may be due to different melt compositions (a natural rhyolite vs. a synthetic haplogranite), the lower water concentration in the melt in our study, 2.6 wt%, to than in the study of Duc-Tin and Keppler, 5.8 wt%, and the pressure of 800 MPa in this study and 200 MPa in that of Duc-Tin and Keppler (2015).

Effect of melt composition on the solubility of monazite and xenotime

Boron. Despite the differences in crystal structure and size of REE incorporated into their lattice, monazite and xenotime exhibit similar low solubilities in silicic melts that are not measurably affected by addition of boron in this study. However, the rhyolitic melt into which these phosphates dissolve is influenced by the combination of dissolving phosphate components and the addition of boron.

The combination of boron-doped silicate melt with dissolving phosphate minerals significantly alters the melt composition in the ~100 μm moat around the dissolving phosphate crystal in the highest temperature experiments of this study. This leads to the formation of phosphate-rich nanoparticles that we interpret as a phosphate melt immiscible with the silicate melt, as discussed above. Because of the strong affinity of

calcium and REE for P, those elements tend to concentrate in the phosphate-rich regions (i.e., Veksler et al. 2012). Even though liquid-liquid immiscibility can also be observed in the boron-free experiments, the boron-bearing melts seem to be more disposed to silicate-phosphate melt immiscibility, because the width of liquid-liquid immiscibility zone is 30 μm in the boron-free experiment and 100 μm in the boron-bearing experiment at the same *P-T* conditions. This suggests that the addition of even small amounts of boron expands the liquid-liquid immiscibility zone.

Many studies on liquid-liquid immiscibility in natural melts have been conducted to explain the genesis of phosphate- and magnetite-rich nelsonites (e.g., Bogaerts and Schmidt 2006; Tollari et al. 2008; Lester et al. 2013; Hou et al. 2018). These studies show that during phase separation of a P-rich melt from a silica-rich melt the iron and calcium preferentially fractionate into the P-rich melt. This affinity is the cause of the uphill diffusion of Fe and Ca seen in Figure 5. Because of the affinity of REE for P they also would fractionate into the phosphate melt (Veksler et al. 2012).

We hypothesize that B enhances phase separation of P-rich melts, similar to those found near the crystals in experiments at 1300 and 1400 °C, from the silicate melts because the presence of boron in silicate melts may cause the disruption of melt structure depending on the coordination state of boron. Structural units containing B(IV) polymerize the network as opposed to units containing B(III). Gan et al. (1994) found that in the presence of P_2O_5 the coordination of B shifts from B(IV) to B(III) in K_2O-B_2O_3-SiO_2-P_2O_5 glasses (Gan et al. 1994). The B(III) species reside outside the silicate network and so does P^{5+}, forming phosphate-rich regions (Gan et al. 1994 and references therein), which could lead to phase separation.

Alkalinity. Montel (1986, 1993) stressed the influence of melt alkalinity on the solubility of monazite. He studied melts in the Na_2O-K_2O-SiO_2-Al_2O_3 system saturated with a synthetic, Ce-monazite at constant *P-T* conditions (200 MPa and 800 °C). His study showed increasing monazite solubility with increasing alkalinity or decreasing ASI index. This correlation was attributed to local charge-balancing of REE^{3+} by non-bridging O atoms in the melt. Addition of alkalis to melts with an ASI of 1 creates additional non-bridging O atoms, and hence the possible correlation between the peralkalinity of the melt and increased monazite solubility (Duc-Tin and Keppler 2015). Similar behavior was seen for xenotime by Duc-Tin and Keppler (2015). The lack of increase in REE solubility in peraluminous melts (ASI > 1) was explained by the fact that REE^{3+} ions have a significantly larger ionic radius than Al^{3+} (e.g., 39 pm for Al^{3+} and 119.6 pm for Ce^{3+}, Shannon 1976) and therefore increasing monazite and xenotime solubility in peraluminous melts is not favored (Duc-Tin and Keppler 2015).

The effect of fluxing components. The presence of volatiles and other fluxing components (H_2O, F, B, etc.) in the melt is known to alter the solubility of different minerals in granitic melts.

The results of Rapp and Watson (1986) showed a strong, positive correlation between the water concentration in the melt and monazite solubility. Figure 13 presents the effect of water concentration on the solubility of monazite at 1000 °C, 800 MPa. Although the study of Rapp and Watson (1986) showed that the addition of water to the melt increases the solubility of monazite, the increasing water concentration between 2 and 6 wt% H_2O does not significantly increase the solubility of monazite by much at constant temperature (Fig. 13, all the calculated solubility products are within the same order of magnitude). The maximum difference between our lowest water concentration (2.6 wt% water) and the results of Rapp and Watson (1986) at 6 wt% water is a factor of 2.

Keppler (1993) and Duc-Tin and Keppler (2015) studied the effect of 0–6 wt% fluorine in iron-free, haplogranitic melts. They concluded that fluorine has no influence on the solubility of monazite or xenotime.

Iron. Many of the fundamental studies used simple systems to measure monazite solubility (Montel 1986, 1993; Keppler 1993; Duc-Tin and Keppler 2015). Importantly, these systems lacked iron, which although not an ESC for many REE-rich minerals, may play a role in their crystallization. The concentration of iron was demonstrated to influence zircon saturation in felsic melts (Baker et al. 2002), and we suggest that it may play a similar role for REE-rich minerals. The differences between the results of this study, Rapp and Watson (1986) and Duc-Tin and Keppler (2015) may be due to the presence of iron, and other minor elements, in the natural composition used in this study and in Rapp and Watson, but absent in the synthetic starting materials of Duc-Tin and Keppler (2015).

The oxidation state of iron also may play a significant role in controlling the saturation of the REE-rich minerals found in felsic rocks because ferric iron can be a network former and ferrous iron a network modifier (Mysen and Richet 2005). Differing effects of ferric vs. ferrous iron on the saturation of zircon were proposed by Baker et al. (2002). Thus, even with the same total iron concentration, metaluminous, or peraluminous melts with higher concentrations of ferrous iron may require higher concentrations of REEs for minerals such as monazite to crystallize, whereas higher concentrations of ferric iron may result in saturation of monazite at lower REE concentrations (cf. Baker et al. 2002).

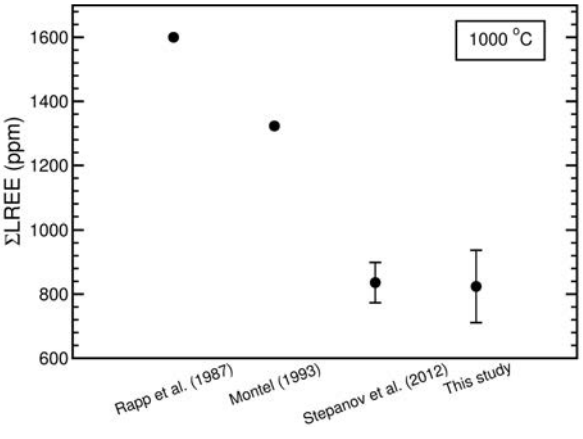

Figure 12. Comparison of the calculated concentrations of the sum ΣLREE in a melt saturated with monazite at 1000 °C, 800 MPa with 3.2 wt% H_2O using published models (Rapp et al. 1987; Montel 1993; Stepanov et al. 2012) with the measured value of this study.

Implications for silicic magmatic systems

Equilibrium monazite and xenotime saturation in silicic magmatic systems

As discussed above, the solubility of monazite and xenotime in this study display the same (within uncertainty) dependence on temperature. When models for monazite solubility are compared with the values obtained from the experiments for xenotime, the concentration value of Y at xenotime saturation agrees within with [ΣLREE] value of Stepanov et al. (2012) for monazite to within uncertainty. This suggests that the same models used for monazite solubility can be used for xenotime solubility by replacing [ΣLREE] with [Y]. Monazite solubility was proposed as a possible magmatic geotheromometer (Montel 1993; Skora and Blundy 2012; Stepanov et al. 2012; Duc-Tin and Keppler 2015) and the relationship between temperature and xenotime solubility creates the possibility of using xenotime in the same manner. The solubility of monazite and xenotime exhibit the same reliance on temperature, which indicates that at equilibrium the crystallization of monazite vs. xenotime will only depend on the availability of LREE, P, and Y/HREE. Most granitic rocks have a LREE/(Y+HREE) ratio higher than 1 (calculated from REE concentrations in parts per million, GeoRoc database, http://georoc.mpch-mainz.gwdg.de/georoc/, accessed Dec. 4, 2018) suggesting that monazite should crystalize before xenotime.

Wark and Miller (1993) studied the behavior of accessory minerals in the Sweetwater Wash pluton (California, U.S.A.); they noted that the bulk melt was saturated in monazite throughout differentiation and that monazite crystallization buffered the concentration of LREE. Xenotime crystallizes as a late phase in the pluton, when sufficient concentrations of its ESCs are reached, and controls the abundance of HREE. Hulsbosch et al. (2014) showed a similar behavior of early crystalizing monazite controlling the abundance of LREE in pegmatites from Gatumba (Rwanda). In their case, however, the late-crystallizing phases controlling the concentrations of HREE are apatite, columbite-group minerals and beryl, not xenotime.

The results of this study suggest that the explanation for fractionation of HREE/Y from LREE and delayed crystallization of HREE-bearing minerals results from competition between monazite and Y/HREE-rich minerals. The solubility of monazite and xenotime are the same within uncertainty, which leads to the hypothesis that the early crystallization of monazite was driven by the availability of LREE and that the concentration of Y and/or HREE was not sufficient to crystalize xenotime during the early stages of crystallization. Xenotime crystalizes as a late stage phase in the Sweetwater Wash pluton, which implies that significant crystallization had to occur to drive the phosphorus and Y/HREE concentrations in the melt to the necessary levels for its saturation. In Gatumba, phosphorus was still available (evidenced by the crystallization of apatite) during late-stage crystallization, but Y and HREE were incorporated into other minerals, which may indicate that the concentrations of Y and HREE were not sufficient for crystallization of xenotime before the melt became saturated in apatite, columbite-group minerals and beryl.

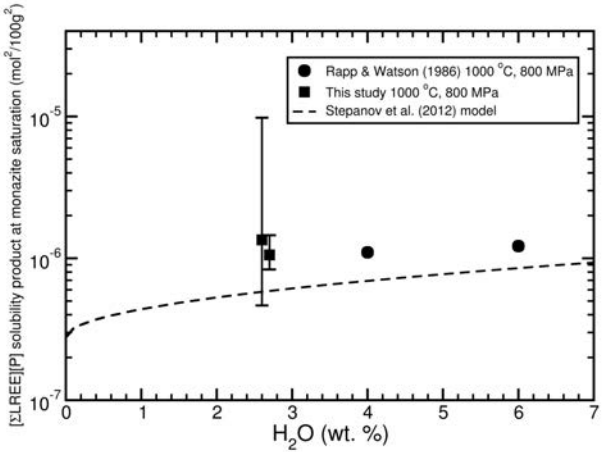

Figure 13. The effect of water concentration on the solubility of monazite at 1000 °C, 800 MPa, based upon this study, Rapp and Watson (1986), and the monazite solubility model of Stepanov et al. (2012).

Disequilibrium during rapid crystal growth

Harrison and Watson (1984) convincingly demonstrated that an accessory phase can crystallize even when the bulk melt is not saturated with that phase. Accessory phases can crystallize from a limited melt volume that reaches saturation due to the so-called "snow plow" effect (i.e., Smith et al. 1955; Harrison and Watson 1984; Rapp and Watson 1986; Holycross and Watson 2018). This effect occurs when incompatible trace elements rejected by a crystallizing phase (e.g., feldspar) build up in front of fast-growing crystal faces causing local saturation because diffusion cannot rapidly transport these incompatible elements away from the advancing crystal face. If the "snow plow" effect dominantly controlled crystallization of REE-rich minerals in felsic systems, then correlations between bulk-rock concentrations of REE and of other elements might be substantially different than observed in equilibrium experiments. However, in such a case REE-rich mineral should be found as inclusions within more-common silicate minerals, such as feldspars and quartz, or trapped at boundaries between them.

Diffusion of Y is two orders of magnitude greater than LREE, suggesting the possibility of diffusive fractionation between these elements. Figure 14 shows the diffusive separation of faster diffusing Y from slower diffusing Ce (representing LREE) at a pile-up in front of a growing K-feldspar (at growth rate of 10^{-9} m/s) at 700 °C with the initial concentration of 50 ppm for both Y and Ce. The partition coefficients between high silica rhyolite and K-feldspar used in the model are 0.095 for Ce (Stix and Gorton 1990, GERM database, https://earthref.org/GERM/, accessed Nov. 21, 2018), and 0.067 for Y (Ewart and Griffin 1994, GERM database, accessed Nov. 21, 2018). The simulation of the pile-up, based on a model first developed by Smith et al. (1955, Eq. 26 therein) was performed for a duration of 10 000 s. Assuming sufficient P, both monazite and xenotime would crystallize in close association (the concentration of Ce at monazite saturation in the model is reached only a few micrometers before the concentration of Y at xenotime saturation), however if the P concentration was insufficient, monazite would crystallize first because of yttrium's more rapid diffusion away from the crystallization front; this yttrium is expected to be later incorporated into non-phosphate minerals or into xenotime

if there was another pile-up after LREE were depleted and if sufficient phosphorus remained in the melt. This process could explain the appearance of xenotime and monazite in biotite that Wark and Miller (1993) found in the Sweetwater Wash pluton and interpreted as the result of local saturation.

Liquid-liquid immiscibility

Even small additions of boron to P- and Fe-bearing silicate melts appear to promote liquid-liquid phase separation. The presence of boron affects the melt structure and locally creates favorable sites for the REE and/or Ca. The formation of liquid-liquid immiscibility, however, requires high phosphorus concentrations. In our study, the immiscibility zone is only visible at 1300 and 1400 °C where the P concentration at saturation is above 1 wt% P_2O_5. It is not observable at lower temperatures where the maximum concentration of P_2O_5 in monazite- or xenotime-saturated rhyolitic melts is 0.4 wt% P_2O_5. It is therefore expected that liquid-liquid immiscibility would become a significant fractionation mechanism in magmatic systems only when the P concentration exceeds 0.4 wt%.

One example where natural evidence of liquid-liquid immiscibility involving silicic melts and phosphate- and REE-rich melts may be REE-rich segregations seen in some in aplite dikes. Stern et al. (2018) studied fluoride-, phosphate- and REE-rich globular segregations occurring in aplite dikes intruding the Longs Peak-St. Vrain Silver Plume-type granite batholith near Jamestown, Colorado. They interpreted the segregations and the aplites as having been formed from coexisting immiscible liquids and suggest that their observations support the premise that immiscible liquids may play a significant role in concentrating REE in silicic magmatic systems. Although the system described by Stern et al. (2018) differs from our experiments, mainly due to the high fluorine content of 5–8 wt%, the P_2O_5 concentrations in the REE-rich globular segregations are similar to our experiments in the immiscibility zone at 1400 °C, 3.7–4.8 wt% P_2O_5. The concentration of P_2O_5 in bulk sample of aplite + the REE-rich segregations is 0.46 wt%, which is slightly above the P_2O_5 concentration below which, in our experiments, we no longer observe liquid-liquid immiscibility (0.4 wt%). Although our experiments with liquid-liquid immiscibility were at much higher temperature, they still provide supporting evidence for the conclusion of Stern et al. (2018) that silicate-phosphate liquid-liquid immiscibility may play the important role of concentrating REE in some magmatic systems. We hypothesize that the addition of significant concentrations of fluorine, similar to those measured by Stern et al. (2018), will expand the phosphate-silicate liquid-liquid immiscibility field seen in our boron-bearing experiments to lower temperatures where it may be a petrogenetically important process in some circumstances.

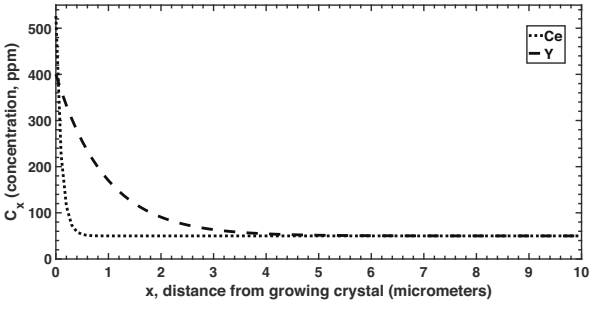

Figure 14. Diffusive separation in front of a growing crystal following Smith et al. (1955, their Eq. 26) of faster diffusing Y from slower diffusing Ce (representing LREE) at a pile-up in front of a K-feldspar (at growth rate of 10^{-9} m/s) at 700 °C with an initial concentration of 50 ppm in the melt for both Y and Ce. The partition coefficients between high silica rhyolite and K-feldspar used in the model are 0.095 for Ce (Stix and Gorton 1990, GERM database, https://earthref.org/GERM/, accessed Nov. 21, 2018), and 0.067 for Y (Ewart and Griffin 1994, GERM database, accessed Nov. 21, 2018); duration is 10 000 s.

Acknowledgments and Funding

We thank Youxue Zhang and an anonymous reviewer for their thorough reviews and E. Bruce Watson for editorial handling of this manuscript. We extend our gratitude to Lang Shi and Glenn Poirier for their assistance with EPMA analyses and to André Poirier for help with LA-ICP-MS analyses. This research was funded by the National Sciences and Engineering Council (NSERC) of Canada Discovery grant awarded to D.R.B.

References cited

Asami, M., Suzuki, K., and Grew, E.S. (2002) Chemical Th–U–total Pb dating by electron microprobe analysis of monazite, xenotime and zircon from the Archean Napier Complex, East Antarctica: evidence for ultra-high-temperature metamorphism at 2400 Ma. Precambrian Research, 114, 249–275.

Baker, D.R., Conte, A., Freda, C., and Ottolini, L. (2002) The effect of halogens on Zr diffusion and zircon dissolution in hydrous metaluminous granitic melts. Contributions to Mineralogy and Petrology, 142, 6, 666–678.

Bartels, A., Behrens, H., Holtz, F., Schmidt, B.C., Fechtelkord, M., Knipping, J., Crede, L., Baasner, A., and Pukallus, N. (2013) The effect of fluorine, boron and phosphorus on the viscosity of pegmatite forming melts. Chemical Geology, 346, 184–198.

Bea, F. (1996) Residence of REE, Y, Th and U in granites and crustal protoliths; Implications for the chemistry of crustal melts. Journal of Petrology, 37, 3, 521–552.

Behrens, H., Roux, J., Neuville, D.R., and Siemann, M. (2006) Quantification of dissolved H_2O in silicate glasses using confocal microRaman spectroscopy. Chemical Geology, 229, 96–112.

Berner, R.A. (1968) Rate of concretion growth. Geochimica et Cosmochimica Acta, 32, 477–483.

Bogaerts, M., and Schmidt, M.W. (2006) Experiments on silicate melt immiscibility in the system Fe_2SiO_4-$KAlSi_3O_8$-SiO_2-CaO-MgO-TiO_2-P_2O_5 and implications for natural magmas. Contributions to Mineralogy and Petrology, 152, 257–274.

Chorlton, L.B., and Martin, R.F. (1978) Effect of boron on the granite solidus. Canadian Mineralogist, 16, 239–244.

Crank, J. (1975). The Mathematics of Diffusion. Clarendon Press, Oxford.

Dalpé, C., and Baker, D.R. (2000) Experimental investigation of large-ion-lithophile-element-, high-field-strength-element- and rare-earth-element-partitioning between calcic amphibole and basaltic melt: the effects of pressure and oxygen fugacity. Contributions to Mineralogy and Petrology, 140, 233–250.

Dingwell, D.B., Knoche, R., Webb, S.L., and Pichavant, M. (1992) The effect of B_2O_3 on the viscosity of haplogranitic liquids. American Mineralogist, 77, 457.

Duc-Tin, Q., and Keppler, H. (2015) Monazite and xenotime solubility in granitic melts and the origin of the lanthanide tetrad effect. Contributions to Mineralogy and Petrology, 169, 1, 1–26.

Ercit, T.S. (2005). REE–enriched granitic pegmatites. In R.L. Linnen and I.M. Sampson, Eds., Rare-Element Geochemistry and Mineral Deposits. Geological Society of Canada Short Course Notes, St. Catharines, 17, 175–199.

Ewart, A., and Griffin, W.L. (1994) Application of proton-microprobe data to trace-element partitioning in volcanic rocks. Chemical Geology, 117, 251–284.

Fortin, M-A., Riddle, J., Desjardins-Langlais, Y., and Baker, D.R. (2015) The effect of water on the sulfur concentration at sulfide saturation (SCSS) in natural melts. Geochimica et Cosmochimica Acta, 160, 100–116.

Gan, H., Hess, P.C., and Kirkpatrick, R.J. (1994) Phosphorus and boron speciation in K_2O-B_2O_3-P_2O_5 glasses. Geochimica et Cosmochimica Acta, 58, 4633–4647.

Guastoni, A., Secco, L., Pennacchioni, G., Nestola, F., Pozzi, G., Schiazza, M., and Fioretti, A.M. (2016) Monazite-(Ce) and xenotime-(Y) from an LCT, NYF tertiary pegmatite field: Evidence from a regional study in the central alps (Italy and Switzerland). Canadian Mineralogist, 54, 4, 863–877.

Guo, C., and Zhang, Y. (2016) Multicomponent diffusion in silicate melts: SiO_2-TiO_2-Al_2O_3-MgO-CaO-Na_2O-K_2O system. Geochimica et Cosmochimica Acta, 195, 126–141.

——— (2018) Multicomponent diffusion in basaltic melts at 1350 °C. Geochimica et Cosmochimica Acta, 228, 190–204.

Harrison, T.M., and Watson, E.B. (1984) The behavior of apatite during crustal anatexis: Equilibrium and kinetic considerations. Geochimica et Cosmochimica Acta, 48,

7, 1467–1477.
Holtz, F., Dingwell, D.B., and Behrens, H. (1993) Effects of F, B_2O_3 and P_2O_5 on the solubility of water in haplogranite melts compared to natural silicate melts. Contributions to Mineralogy and Petrology, 113, 492–501.
Holycross, M.E., and Watson, E.B. (2018) Trace element diffusion and kinetic fractionation in wet rhyolitic melt. Geochimica et Cosmochimica Acta, 232, 14–29.
Hou, T., Charlier, B., Holtz, F. Veksler, I., and Zhang, Z., Thomas, R., and Namur, O. (2018). Immiscible hydrous Fe–Ca–P melt and the origin of iron oxide-apatite ore deposits. Nature Communications, 9.
Hudon, P., Baker, D.R., and Toft, P.B. (1994) A high-temperature assembly for 1.91-cm (3/4-in.) piston-cylinder apparatus. American Mineralogist, 79, 145–147.
Hulsbosch, N., Hertogen, J., Dewaele, S., and Muchez, P. (2014) Alkali metal and rare earth element evolution of rock-forming minerals from the Gatumba area pegmatites (Rwanda): Quantitative assessment of crystal-melt fractionation in the regional zonation of pegmatite groups. Geochimica et Cosmochimica Acta, 132, 349–374.
Keppler, H. (1993) Influence of fluorine on the enrichment of high field strength trace elements in granitic rocks. Contributions to Mineralogy and Petrology, 114, 4, 479–488.
Lester, G.W., Clark, A.H., Kyser, T.K., and Naslund, H.R. (2013). Experiments on liquid immiscibility in silicate melts with H_2O, P, S, F and Cl: implications for natural magmas. Contributions to Mineralogy and Petrology, 166, 329–349.
Li, Q.L., Li, X.H., Lan, Z.W., Guo, C.L., Yang, Y.N., and Tang, G.Q. (2013) Monazite and xenotime U-Th-Pb geochronology by ion microprobe: dating highly fractionated granites at Xihuashan tungsten mine, SE China. Contributions to Mineralogy and Petrology, 166, 65–80.
Liang, Y. (2010) Multicomponent diffusion in molten silicates: theory, experiments, and geological applications. Reviews in Mineralogy and Geochemistry, 72, 409–446.
Miller, C.F., and Mittlefehldt, D.W. (1982) Depletion of light rare-earth elements in felsic magmas. Geology, 10, 3, 129.
——— (1983) Geochemistry of the Sweetwater Wash Pluton, California: implication for "anomalous" trace element behaviour during differentiation of felsic magmas. Geochimica et Cosmochimica Acta, 47, 109–124.
Montel, J.-M. (1986) Experimental determination of the solubility of Ce-monazite in SiO_2-Al_2O_3-K_2O-Na_2O melts at 800 °C, 2 kbar, under H_2O-saturated conditions. Geology, 14, 8.
——— (1993) A model for monazite/melt equilibrium and application to the generation of granitic magmas. Chemical Geology, 110, 1, 127–146.
Mungall, J.E., Dingwell, D.B., and Chaudisson, M. (1999) Chemical diffusivities of 18 trace elements in granitoid melts. Geochimica et Cosmochimica Acta, 63, 2599–2610.
Mysen, B.O., and Richet, P. (2005) Silicate Glasses and Melts: Properties and structure. Elsevier, Amsterdam.
Ni, Y., Hughes, J.M., and Mariano, M.N. (1995) Crystal chemistry of the monazite and xenotime structures. American Mineralogist, 80, 21–26.
Paton, C., Hellstrom, J., Bence, P., Woodhead, J., and Hergt, J. (2011) Iolite: Freeware for the visualization and processing of mass spectrometric data. Journal of Analytical Atomic Spectrometry, 26, 2508–2518.
Pichavant, M. (1981) An experimental study of the effect of boron on a water saturated haplogranite at 1 kbar vapour pressure. Contributions to Mineralogy and Petrology, 76, 430–439.
——— (1987) Effects of B and H_2O on liquidus phase relations in the haplogranite system at 1 kbar. American Mineralogist, 72, 1056–1070.
Rapp, R.P., and Watson, E.B. (1986) Monazite solubility and dissolution kinetics: implications for the thorium and light rare earth chemistry of felsic magmas. Contributions to Mineralogy and Petrology, 94, 3, 304–316.
Rapp, R.P., Ryerson, F.J., and Miller, C.F. (1987) Experimental evidence bearing on the stability of monazite during crustal anatexis. Geophysical Research Letters, 14, 307–310.
Shannon, R.D. (1976) Revised effective radii and systematic studies of interatomic distances in halides and chalcogenides. Acta Crystallographica, 32, 751–767.
Silva, E.N., Ayala, A.P., Guedes, I., Paschoal, C.W.A., Moreira, R.L., Loong, C.K., and Boatner, L.A. (2006) Vibrational spectra of monazite-type rare-earth orthophosphates. Optical Materials, 29, 224–230.
Simmons, W.B., Falster, A., Webber, K.L., Roda-Robles, E., Boudreaux, A.P., Grassi, L.R., and Freeman, G. (2016) Bulk composition of Mt. Mica pegmatite, Maine, USA: implications for the origin of an LCT type pegmatite by anatexis. Canadian Mineralogist, 54, 1053–1070.
Skora, S., and Blundy, J. (2012) Monazite solubility in hydrous silicic melts at high pressure conditions relevant to subduction zone metamorphism. Earth and Planetary Science Letters, 321-322, 104–114.
Smith, V.G., Tiller, W.A., and Rutter, J.W. (1955) A mathematical analysis of solute redistribution during solidification. Canadian Journal of Physics, 33, 723–745.
Stepanov, A.S., Hermann, J., Rubatto, D., and Rapp, R.P. (2012) Experimental study of monazite/melt partitioning with implications for the REE, Th and U geochemistry of crustal rocks. Chemical Geology, 300-301, 200–220.
Stern, C.R., Allaz, J.M., Raschke, M.B., Farmer, G.L, Skewes, M.A., and Ross, J.T. (2018). Formation by silicate-fluoride+phosphate melt immiscibility of REE-rich globular segregations within aplite dikes. Contributions to Mineralogy and Petrology, 173, 65.
Stix, J., and Gorton, M.P. (1990) Variations in trace element partition coefficients in sanidine in the Cerro Toledo Rhyolite, Jemez Mountains, New Mexico: Effects of composition, temperature, and volatiles. Geochimica et Cosmochimica Acta, 54, 2697–2708.
Sun, S.S., and Hanson, G.N. (1975) Origin of Ross Island basanitoids and limitations upon the heterogeneity of mantle sources for alkali basalts and nephelinites. Contributions to Mineralogy and Petrology, 52, 2, 77–106.
Suzuki, K., and Kato, T. (2008) CHIME dating of monazite, xenotime, zircon and polycrase: Protocol, pitfalls and chemical criterion of possibly discordant age data. Gondwana Research, 14, 569–586.
Tollari, N., Baker, D.R., and Barnes, S.-J. (2008) Experimental effects of pressure and fluorine on apatite saturation in mafic magmas, with reference to layered intrusions and massif anorthosites. Contributions to Mineralogy and Petrology, 156, 161–175.
Veksler, I.V., Dorfman, A.M., Dulski, P., Kamenetsky, V.S., Danyushevsky, L.V., Jeffries, T., and Dingwell, D.B. (2012) Partitioning of elements between silicate melt and immiscible fluoride, chloride, carbonate, phosphate and sulphate melt, with implications to the origin of natrocarbonatite. Geochimica et Cosmochimica Acta, 79, 20–40.
Wark, D.A., and Miller, C.F. (1993) Accessory mineral behavior during differentiation of a granite suite: monazite, xenotime and zircon in the Sweetwater Wash pluton, southeastern California, U.S.A. Chemical Geology, 110, 49–67.
Watson, E.B. (1982) Basalt contamination by continental crust: some experiments and models. Contributions to Mineralogy and Petrology, 80, 73–87.
Wei, G.C.T., and Wuensch, B.J. (1976) Tracer concentration gradients for diffusion coefficients exponentially dependent on concentration. Journal of the American Ceramic Society, 59, 295–299.

Manuscript received December 17, 2018
Manuscript accepted April 26, 2019
Manuscript handled by E. Bruce Watson

Endnote:

[1]Deposit item AM-19-86931, Supplemental Material. Deposit items are free to all readers and found on the MSA website, via the specific issue's Table of Contents (go to http://www.minsocam.org/MSA/AmMin/TOC/2019/Aug2019_data/Aug2019_data.html).